SANDIA REPORT
SAND2021-11359
Printed September 2021

Sandia National Laboratories

Simulation of Low-Rm physics in complex geometries on GPUs with LGR

David Zwick and Dan Ibanez

Prepared by
Sandia National Laboratories
Albuquerque, New Mexico 87185
Livermore, California 94550

Issued by Sandia National Laboratories, operated for the United States Department of Energy by National Technology & Engineering Solutions of Sandia, LLC.

NOTICE: This report was prepared as an account of work sponsored by an agency of the United States Government. Neither the United States Government, nor any agency thereof, nor any of their employees, nor any of their contractors, subcontractors, or their employees, make any warranty, express or implied, or assume any legal liability or responsibility for the accuracy, completeness, or usefulness of any information, apparatus, product, or process disclosed, or represent that its use would not infringe privately owned rights. Reference herein to any specific commercial product, process, or service by trade name, trademark, manufacturer, or otherwise, does not necessarily constitute or imply its endorsement, recommendation, or favoring by the United States Government, any agency thereof, or any of their contractors or subcontractors. The views and opinions expressed herein do not necessarily state or reflect those of the United States Government, any agency thereof, or any of their contractors.

Printed in the United States of America. This report has been reproduced directly from the best available copy.

Available to DOE and DOE contractors from

U.S. Department of Energy
Office of Scientific and Technical Information
P.O. Box 62
Oak Ridge, TN 37831

Telephone: (865) 576-8401
Facsimile: (865) 576-5728
E-Mail: reports@osti.gov
Online ordering: http://www.osti.gov/scitech

Available to the public from

U.S. Department of Commerce
National Technical Information Service
5301 Shawnee Road
Alexandria, VA 22312

Telephone: (800) 553-6847
Facsimile: (703) 605-6900
E-Mail: orders@ntis.gov
Online order: https://classic.ntis.gov/help/order-methods

ABSTRACT

Efficient modeling of low magnetic Reynolds number (low-Rm) magnetohydrodynamics is often challenging and requires the implementation of innovative techniques to avoid key barriers experienced with prior approaches. We detail a new paradigm for first-principles simulation of the solution to the low-Rm governing equations in complex geometries. As a result of a number of innovative numerical advances, the next-generation GPU (graphics processing unit) accelerated physics code LGR has been successfully applied to the modeling of exploding wire problems.

CONTENTS

LIST OF FIGURES

LIST OF TABLES

1. INTRODUCTION

We are interested in solving the multi-fluid magnetohydrodynamic (MHD) equations, which represent the coupled set of Maxwell's equations and standard hydrodynamic conservation laws for a current-carrying material undergoing phase changes. Based on the relevant length and time scales of applications, a low magnetic Reynolds number approximation can be employed which dramatically simplifies the governing equations [1]. At its essence, the low-Rm approximation involves solving for a background voltage field, allowing current density to diffuse instantaneously, which is then used to Ohmically heat electrically conducting materials.

Attempts at first-principles modeling of low-Rm physics can fail in multiple ways, often stemming from the discretization schemes used to represent problems of interest. Rapid Ohmic heating of materials results in the expansion and subsequent phase change of materials. As a result, traditional Eulerian methods must faithfully represent the electrical conductivities of mixed-material cells. This poses numerous stability and modeling challenges, especially in regions where both conductive and insulating materials are present, whose material conductivities can vary by more than ten orders of magnitude. Alternatively, pure Lagrangian methods will fail due to mesh entanglement as the materials undergo large deformations. Indeed, legacy codes with such approximations, such as ALEGRA [2], struggle with these issues in similar applications.

We circumvent these issues in both unconventional and inventive ways. The Lagrangian Grid Reconnection (LGR) code (formerly called ALEXA) is extended to include the low-Rm MHD approximation. LGR is a GPU-accelerated code developed at Sandia National Laboratories [3]. It uses Lagrangian finite elements to solve hydrodynamic problems and employs sophisticated mesh reconnection and remapping schemes to prevent mesh entanglement even under large deformations. Since LGR uses unstructured finite elements, even complicated geometries can be easily represented with a body fitted mesh. Due to this, mixed-material cells will not exist, alleviating the need for a mixed-material sub-cell representation. Due to its GPU-acceleration, simulations are able to be performed rapidly on desktop-scale hardware like GPU-equipped laptops.

The remainder of this work is organized as follows. First, we give the governing equations and discretization schemes. Particular emphasis is given to the low-Rm extension of LGR. Following this, the low-Rm solver is verified using multiple test problems. Then, the new LGR code is exercised through the modeling and simulation of a laboratory-scale exploding wire. Finally, conclusions are drawn and future work is suggested.

2. GOVERNING EQUATIONS AND METHODS

2.1. Conservation Equations

LGR is a Lagrangian unstructured finite element GPU-accelerated code that solves the governing hydrodynamic conservation of mass, momentum, and energy equations in a given material, along with appropriate stabilization for high strain-rate regions. LGR also contains remap and remesh algorithms to preserve high quality elements and prevent tangling [3].

In this work, we extend the hydrodynamic equations and introduce a low-Rm approximation to solve for a voltage field within materials. The Lagrangian translation and governing conservation of mass, momentum, and energy equations are given by

$$\frac{d\mathbf{X}}{dt} = \mathbf{V}, \tag{1}$$

$$\rho = J^{-1}\rho_0, \tag{2}$$

$$\rho\frac{d\mathbf{V}}{dt} = \nabla\cdot\boldsymbol{\sigma}, \tag{3}$$

$$\rho\frac{de}{dt} = \boldsymbol{\sigma} : \nabla\mathbf{V} + \sigma_e|\nabla\phi|^2, \tag{4}$$

where ρ is the mass density, $\mathbf{X}$ is the node coordinates, $\mathbf{V}$ is the velocity, e is the specific internal energy per unit mass, $\boldsymbol{\sigma}$ is the stress tensor, and J is the determinant of the deformation gradient matrix. These equations are standard in hydrodynamics, with the only difference being the addition of the final term in the energy equation, which is called the *Joule heating* term. This term accounts for the energy added by resistive (or Ohmic) heating due to current crowding in conducting materials and contains both the electrical conductivity σ_e and the voltage field ϕ. The density and internal energy are used as coordinates in a tabular lookup which provides both the pressure (hydrostatic portion of the stress tensor) and the electrical conductivity. The remainder of the stress tensor also contains artificial viscosity terms that help stabilize the solution [3].

The low-Rm approximation additionally entails solving for the voltage from the following Laplace system

$$\nabla\cdot(\sigma_e\nabla\phi) = 0, \tag{5}$$

with Dirichlet boundary conditions on ϕ corresponding to applied electrical voltage potentials at representative anode and cathode boundaries. We note that since the material properties are transient, solution of the voltage system in (5) is required at every time step in the solution procedure.

It is also noted that the magnetic Reynolds number is defined by $R_m = \mu_0\sigma_e LU$, where μ_0 is the magnetic permeability of free space ($\approx 1.2566\times10^{-6}$ H/m), L is a reference length scale, and U is a reference velocity scale. The magnetic Reynolds number is a measure of the relative effects of magnetic induction to diffusion. For $R_m \ll 1$, magnetic diffusion is rapid compared to the advective timescale and the low-Rm approximation is valid.

2.2. Discretizations

In order to advance the simulation in time, a Verlet time integration scheme is used [4]. A brief summary of the time integration scheme is given below to advance from a time step n to time step $n+1$ in Algorithm 1.

The procedure follows the typical Verlet integration scheme applied to hydrodynamics. In this work we have added additional steps related to the low-Rm approximation which includes steps 8, 9, 10, and 15. Note that $\tilde{e}$ in the algorithm denotes a predicted internal energy value at the next time step. Using a tabulated equation of state, the next time step's density and predicted internal energy are used to compute the material properties of pressure and electrical conductivity as seen in steps

Algorithm 1 Verlet time integration scheme with low-Rm additions.

1: **procedure** VERLET INTEGRATION SCHEME
2: Calculate midpoint velocity $\mathbf{V}^{n+1/2}$
3: Calculate next time step states
4: Position $\mathbf{X}^{n+1}$ ▷ use $\mathbf{V}^{n+1/2}$
5: Density ρ^{n+1} ▷ use ρ^n and $\mathbf{X}^{n+1}$
6: Predicted energy $\tilde{e}^{n+1}$ ▷ use $\dot{e}^n$
7: Pressure P^{n+1} ▷ use ρ^{n+1} and $\tilde{e}^{n+1}$
8: Electrical conductivity σ_e^{n+1} ▷ use ρ^{n+1} and $\tilde{e}^{n+1}$
9: Voltage ϕ^{n+1} ▷ solve (5) with σ_e^{n+1}
10: Solve electrical circuit
11: Backtrack to midpoint internal energy $e^{n+1/2}$
12: Calculate next time step velocity $\mathbf{V}^{n+1}$
13: Calculate next time step energy rate $\dot{e}^{n+1}$
14: Stress power ▷ $\boldsymbol{\sigma}^{n+1} : \nabla \mathbf{V}^{n+1}$
15: Joule heating rate ▷ $\sigma_e^{n+1} |\nabla \phi^{n+1}|^2$
16: Calculate next time step energy ▷ use $\dot{e}^{n+1}$
17: **end procedure**

7 and 8. The electrical conductivity is then used to calculate the voltage field from the low-Rm system in (5). As will be discussed later, the voltage field and conductivity are used to provide a lumped total electrical resistance in an electrical circuit in step 10. Finally, the Joule heating rate is added to the stress power in step 15 to advance to the next time step's internal energy in step 16.[1]

The spatial discretization consists of Lagrangian finite elements as detailed in [3]. In particular, linear simplex elements are used that include bar, triangle, and tetrahedral elements. The kinematic variables, such as position and velocity, are located at the element nodes while the thermodynamic variables reside at element centers. In order to extend the governing equations to the added low-Rm physics, we choose to additionally store the electrical conductivity with the thermodynamic variables at element centers and collocate the voltage field at the nodes. This choice results in a straightforward calculation of the Joule heating term in (4) since the linear elements result in constant gradients within each element.

While assembly of the conservation equations in the global finite element system remains unchanged, further explanation regarding the assembly of the voltage system in (5) for GPU's is required. At the most basic level, application of the Galerkin finite element methodology to (5) requires the assembly of a global stiffness matrix $\mathbf{S}$, to which the solution of the semi-discrete system with appropriate boundary conditions

$$\mathbf{S}\phi = \mathbf{0}, \tag{6}$$

results in the nodal voltages ϕ.[2] The global stiffness matrix is composed of local element stiffness

[1] Note that $\dot{e}$ represents the right-hand side forcing of the energy equation (4).

[2] The appropriate boundary conditions on the voltage field consist of Dirichlet voltages along the corresponding geometric boundaries representing anode and cathode circuit terminals.

matrices $\mathbf{s}$ given by

$$\mathbf{s}_{ij} = \int \sigma_e \nabla N_i \cdot \nabla N_j d\mathcal{V}, \tag{7}$$

where σ_e is an individual element's electrical conductivity, $\mathcal{V}$ is the element's volume (or area in two-dimensions), and N_k are the standard linear finite element shape functions. The global stiffness matrix is assembled through summation of the N_E total element stiffness matrices given by

$$\mathbf{S}_{IJ} = \sum_{k=1}^{N_E} \mathbf{s}_{ij}^k, \tag{8}$$

with a known local to global node mapping M, such that for a local node l of element k, the global node L specifies the location in the global stiffness matrix by $M(l,k) \rightarrow L$.

The difficultly in on-device GPU assembly of the global stiffness matrix from the individual element stiffness matrices is now observed since naive summation of the element matrices would result in severe race conditions. A first order attempt to remedy this would require atomic addition so that (8) does not result in a race condition if parallelized directly over elements. However, atomic addition will result in non-deterministic behavior of the program. We consider an alternative approach that takes advantage of the pattern formed in the local element stiffness matrix when simplex elements are used. The pattern is demonstrated for a two-dimensional element in Figure 2-1.

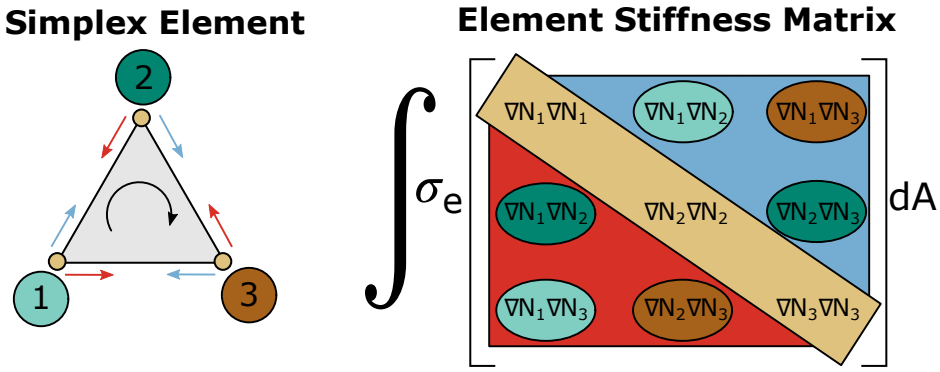

Figure 2-1 Example of pattern used in GPU assembly of element stiffness matrix.

The triangle element in Figure 2-1 has its nodes ordered clockwise. Each element stiffness matrix has both diagonal and off-diagonal terms. The diagonal terms contain the squared values of the gradients of the element shape functions. The off-diagonal terms are symmetric and contain cross multiplication of the different shape function gradients.

At its core, our chosen assembly pattern relies on the fact that for simplices, the number of edges of an element will be equal to the number of unique off-diagonal entries in the stiffness matrix.[3] As a result, the local stiffness matrices can be fully filled by looping through an element's nodes as

[3]That is, 1, 3, and 6 entries in one, two, and three-dimensions.

shown in Figure 2-1. For each node, the connected edges (two for each node in two-dimensions), which are represented by each of the arrows pointing away from each node, are then looped over. The local node numbers on either side of an edge correspond to the shape function gradient that is used. If the direction of the edge is aligned with the original element's node numbering (clockwise in this example), then it is placed in the upper portion of the stiffness matrix. Accordingly, edge directions opposing the element's node numbering are placed in the lower portion of the matrix. For example, beginning with node 1, edge $\overline{12}$ is aligned with the local node numbering so it corresponds to $\mathbf{s}_{12}$ while edge $\overline{13}$ is opposite the numbering so that it corresponds to $\mathbf{s}_{31}$. Following this, the remaining off-diagonal local element stiffness matrix terms can be filled in. The remaining diagonal components can then be computed by evaluating the squared shape function gradients at each of the local nodes. Finally, the electrical conductivity is evaluated for each element and the integration is performed for every entry in the local stiffness matrix.[4]

Using this pattern, only three GPU kernels are required to assemble the global stiffness matrix. Consider a global finite element mesh which contains N_E elements, N_n nodes, and N_e edges. For each element, let there be n_n nodes per element and n_e edges per element. For simplex elements, n_n is equal to the total number of diagonal element stiffness matrix terms and n_e is equal to the unique number of off-diagonal elements due to symmetry. The three kernels used for the global stiffness matrix assembly are then:

1. Element stiffness matrix assembly:
   In this kernel we loop over elements and store the $N_E \times (n_n + n_e)$ values corresponding to each element's unique local stiffness matrix entries.

2. Contribution of local element diagonal entries:
   The diagonal terms of elements that share the same global nodes are added together and reduced. This kernel involves looping through the global nodes N_n and summing the diagonal values from connected elements that were computed in kernel 1.

3. Contribution of local element off-diagonal entries:
   The off-diagonal terms of elements which share the same global edges are added together and reduced. This kernel involves looping through the global edges N_e and summing the off-diagonal values from connected elements that were computed in kernel 1.

In the present implementation, an additional fourth kernel is used in which the N_n diagonal terms and N_e off-diagonal terms are copied to a sparse matrix that is represented by a connected graph. However, this fourth kernel does not require additional computation. In this way, no race conditions are realized while the global matrix assembly can be performed fully on the GPU. Following the global matrix assembly, the Dirichlet boundary conditions on ϕ are applied and a GPU-based conjugate gradient solver with diagonal preconditioning is used to solve the final system for the nodal voltages to appropriate tolerances.

[4] While the present example is given for a triangular element the same assembly pattern is true of simplex-type elements in other dimensions.

2.3. Equations of State

As previously described, tabulated equations of state are used to represent materials in the system. In the present work, we consider two types of equations of state: (i) thermodynamic and (ii) electrical. Both types of equations of state require specification of two thermodynamic variables in order to obtain a third variable. Typically, the input variables are the density ρ and specific internal energy e. In the case of (i), the thermodynamic quantity of interest is the pressure, which is used for closure of the stress tensor σ by defining its diagonal components (see step 7 in Algorithm 1). In the case of (ii), the quantity of interest is the electrical conductivity, which is used to solve the low-Rm voltage system in (5) (see steps 8 and 9 in Algorithm 1). In the present work, we use two databases which define the equation of state tables, which are SESAME [5] and UTri [6]. The SESAME tables are split apart into two separate tables for the thermodynamic and electrical properties. The tables consist of a rectilinear grid of data which is bilinearly interpolated to each element's particular thermodynamic states. In the UTri database, the thermodynamic and electrical properties reside in a single table. In this model, the table is composed of a triangulation of thermodynamic states which are linearly interpolated to each element's thermodynamic and electrical variables.

2.4. Circuit Discretization

As previously mentioned, the solution of the low-Rm approximation yields a voltage field within the materials under consideration. This approximation is coupled with an external driving circuit which provides electrical energy that heats the materials (Joule heating). In the present circuit model, the materials are treated as a lumped circuit element which acts as a time-varying resistor within the circuit. Additionally, a typical circuit may also consist of other passive circuit elements (resistors, capacitors, and inductors) and can be driven by either a voltage or current source. As shown in Algorithm 1, the circuit is first solved in step 10 which happens after the voltage field has been advanced to the next time step. In order to numerically solve the circuit, modified nodal analysis is used [7]. In modified nodal analysis, a system of linear equations is assembled that accounts for both the current and voltage at all non-ground circuit nodes according to Kirchoff's current and voltage laws. The elementary constitutive laws which relate the current to the voltage for resistors, capacitors, and inductors are given in order below as

$$I = \frac{\Delta V}{R}, \quad I = C\frac{d\Delta V}{dt}, \quad \Delta V = L\frac{dI}{dt},$$

where ΔV is the voltage drop across a circuit element, I is the current through a circuit element, and R, C, and L are the resistance, capacitance, and inductance of each element. Since the capacitor's and inductor's constitutive models each require the evaluation of a time derivative, we use a first order accurate forward Euler approximation to discretize the derivatives.

In the lumped element circuit model, the time-varying bulk material resistance of the finite element discretization is required. The bulk resistance is dependent on the instantaneous geometric and thermodynamic states within the modeled materials. To obtain the bulk resistance, it is noted that the electrical power through a resistive material can be determined by multiplying the voltage

drop across the material with the current through the material. Another method for obtaining the electrical power is by multiplying the electric current density magnitude $\sigma_e|\nabla\phi|$ by the electric field magnitude $|\nabla\phi|$ and integrating over the material volume $\mathcal{V}$. Combining both of these approaches with Ohm's law and rearranging, the bulk material resistance R_M is obtained and given by the following equation

$$\frac{1}{R_M(t)} = \int_{\mathcal{V}} \sigma_e \frac{|\nabla\phi|^2}{\Delta V^2} d\mathcal{V}. \tag{9}$$

The material is thus treated as a time-varying resistor within the circuit which gets solved at each time step. For practical purposes, we note that ΔV, which is obtained from the circuit, can be thought of as a normalizing factor on the voltage field ϕ. As a result, the bulk material resistance is independent of the magnitude of voltage drop across the finite element mesh and only dependent on the material properties and problem geometry, which includes the location of applied voltage boundary conditions.

3. VERIFICATION OF LOW-RM IMPLEMENTATION

In order to verify the low-Rm approach, we now turn our attention to testing. The testing in this section is centered around the accurate calculation of the voltage field in (5) through basic problems of interest where analytic solutions of the voltage system exist. These problems are shown in Figure 3-1. The tests increase in complexity from frames (a) to (c) and are described below.

3.1. Linear Multi-Material

The first test problem is shown in the upper left corner of Figure 3-1. The problem entails two cubes of side length L with different electrical conductivities that are joined together. The left boundary of material 1 is fixed at a voltage potential of 1 while the right boundary of material 2 is fixed at a voltage potential of 0. The analytic solution of this problem is C^0 continuous and given by

$$\phi(\mathbf{x}) = \begin{cases} -\dfrac{1}{L\bar{\sigma}}x + 1, & x \leq L \\ \dfrac{1}{L}\left(\dfrac{1}{\bar{\sigma}} - 1\right)(x - 2L), & \text{otherwise} \end{cases}, \tag{10}$$

where $\bar{\sigma} = 1 + \sigma_1/\sigma_2$. Since the solution to this problem is linear within each material, only a single linear element in x is required for each material. This is achieved by splitting each material cube into 6 tetrahedra. For testing, we use $\sigma_1 = 10$, $\sigma_2 = 1$, and $L = 1$. Solving (5), we compute the ℓ_2 error between the mesh and the analytic solution to be machine precision without any additional refinement.

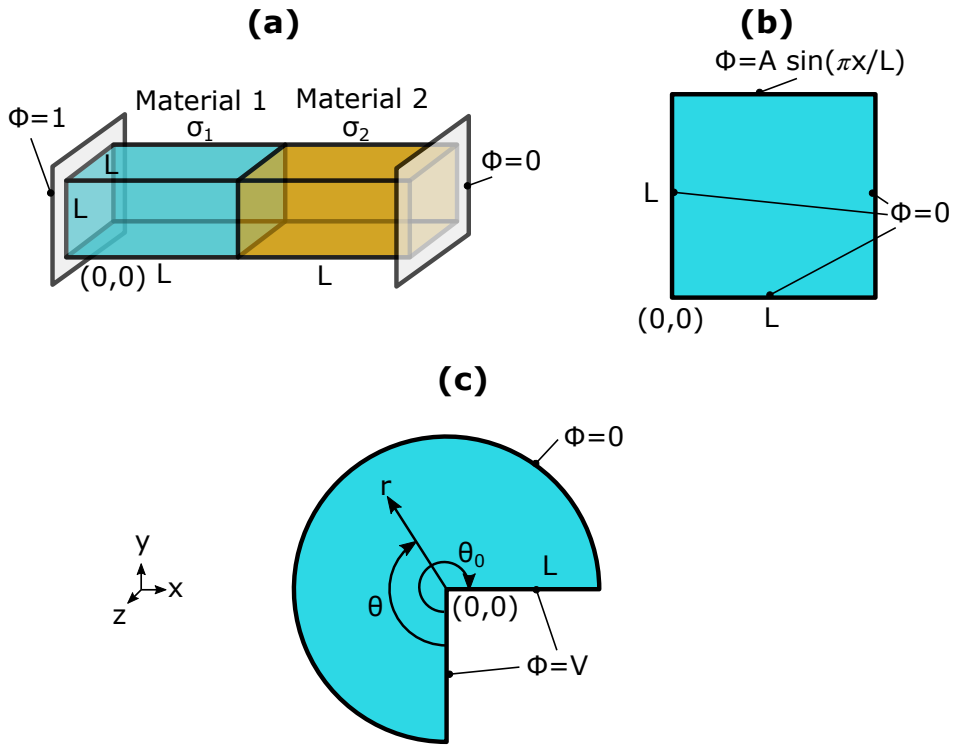

Figure 3-1 Test problems for the low-Rm voltage solver.
The problems include: (a) linear multi-material, (b) sine wave square, and (c) conducting planes in a cylinder.

3.2. Sine Wave Square

The second test problem is a two-dimensional square of length L as shown in the top right corner of Figure 3-1. All boundaries are fixed at zero potential except for the top boundary which is a Dirichlet boundary fixed as a sine wave $\phi = A\sin(\pi x/L)$. The analytic solution within the domain for this case is

$$\phi(\mathbf{x}) = \frac{A}{\sinh(\pi)} \sin\left(\pi\frac{x}{L}\right) \sinh\left(\pi\frac{y}{L}\right). \tag{11}$$

For simplicity, we set the amplitude of the sine wave to be $A = 1$ and the length of the domain to be $L = 1$. A number of calculations were run with LGR at different target mesh resolutions. The ℓ_2 errors between the LGR simulations and the analytic solution were computed and are shown in Figure 3-2. For linear finite elements, the expected convergence rate of Δx^2 is achieved.

3.3. Conducting Planes in a Cylinder

In the third problem in Figure 3-1, we introduce sharp geometrical changes that lead to singularities in (5). The singularities are associated with the electric field $\mathbf{E}$ which is the negative gradient of the computed voltage field. This problem consists of two conducting planes fixed at a potential $\phi = V$

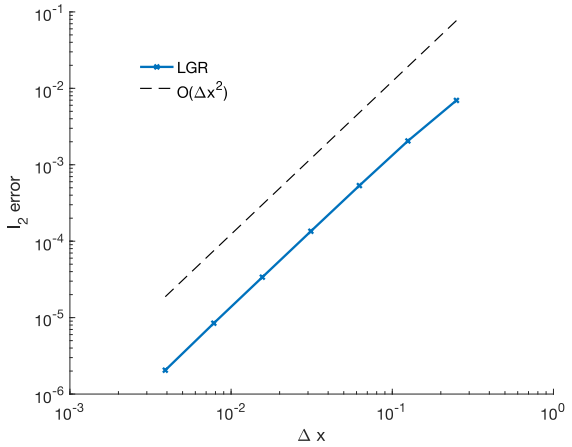

Figure 3-2 Convergence rate for sine wave square geometry problem.

that intersect at an angle θ_0. Enclosing these planes is a cylinder of radius L which is fixed at zero potential. A detailed description of this problem and the asymptotic solution behavior is given in [8] and a brief summary is presented here. Using the polar coordinate system (r,θ) given in the figure, the analytic voltage potential is given by

$$\phi(r,\theta) = V + \sum_{n=1}^{\infty} a_n r^{n\pi/\theta_0} \sin(n\pi\theta/\theta_0), \tag{12}$$

resulting in the electric field $\mathbf{E} = E_r\hat{\mathbf{r}} + E_\theta\hat{\theta}$. Here, $\hat{\mathbf{r}}$ is the unit vector aligned with the radius emanating from the corner origin and $\hat{\theta}$ is its angular complement. The magnitude of the electric field along each unit vector are then given by the infinite summations

$$E_r = -\frac{\pi}{\theta_0} \sum_{n=1}^{\infty} n a_n r^{n\pi/\theta_0 - 1} \sin(n\pi\theta/\theta_0), \tag{13}$$

$$E_\theta = -\frac{\pi}{\theta_0} \sum_{n=1}^{\infty} n a_n r^{n\pi/\theta_0 - 1} \cos(n\pi\theta/\theta_0). \tag{14}$$

Here, a_n represent coefficients obtained by applying the boundary conditions and are given by

$$a_n = \frac{2V}{L^{n\pi/\theta_0}} \left(\frac{\cos(n\pi) - 1}{n\pi} \right). \tag{15}$$

The intersection of the conducting planes and the cylinder at the two points $(0,-L)$ and $(L,0)$ pose an irregularity since the voltage field is doubly defined by the boundary conditions. Here, we arbitrarily set the boundaries to be $\phi = 0$. The effects of this choice are not observed when we set the cylinder radius to be sufficiently large (we use $L = 100$) and focus on the innermost refined region near $(0,0)$. For testing, we set $V = 1$ and $\theta_0 = 3\pi/2$ as shown in the schematic.[5] An angle $\theta = 3\pi/4$ is chosen at which the analytic solution will be compared with the simulation results.

[5]Note the singularity when $r = 0$ at point $(0,0)$ since the power of r in the leading $n = 1$ term is $-1/3$ in (13).

Lastly, the infinite summations are made finite by selecting only the first 13 terms, which represent sufficient convergence in the interval $r \in [0,1]$ with less than $O(10^{-12})$ percent change.

Using these approximations, LGR has been used to solve for the voltage field within the domain at four different mesh resolutions of $\Delta x = 1/10, 1/20, 1/40$, and $1/80$. Here Δx represents the target edge length of the linear triangles that are externally automatically meshed. Due to the linear finite element approximation, the gradients of the voltage field (i.e. the electric field) are constant within each element and discontinuous across elements. The electric field at $\theta = 3\pi/4$ and $r \in [0,1]$ is sampled at each mesh resolution and the results are shown in Figure 3-3 along with the analytic solution.[6] Far from the conducting plane intersection ($r \approx 1$), we observe that LGR reproduces the exact solution remarkably well. However, when we examine the zoomed region near $r = 0$ there is a wider discrepancy between the exact solution and the LGR solutions. In fact, the solution at $r = 0$ is not converging under mesh refinement, which is a direct result of the singularity at the origin due to the sharp intersection of the conducting planes. Despite this, both the analytically diverging solution near the origin and the far field solution appear to be captured with the present methodology, although care must be taken when examining such divergent results in practical applications.

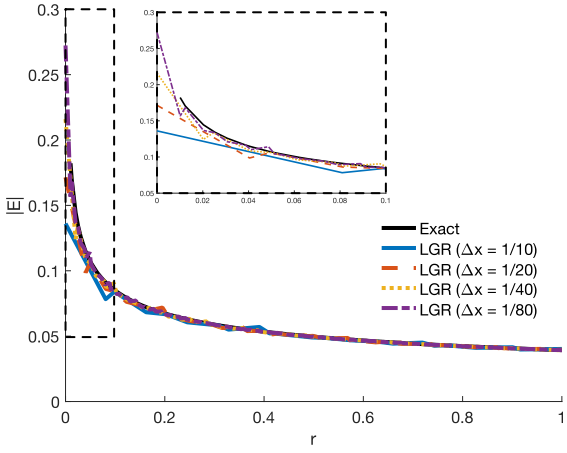

Figure 3-3 Solution to conducting planes in a cylinder problem at different mesh resolutions.

The dashed box shows a zoomed region from $r \in [0, 0.1]$.

4. APPLICATION TO EXPLODING WIRE PROBLEMS

4.1. Simulation Description

Having established confidence in the low-Rm solver, we apply the low-Rm methodology to an exploding wire problem. The exploding wire problem consists of a cylindrical length of wire

[6] Producing a sampling line from 2D triangle elements is performed by ray tracing from $(0,0)$ in the direction $\hat{\mathbf{r}}$. The first point of the line is given the value of the element it is within. The other points are given the value of the cell the line is about to enter.

connected to an electrical circuit which is submerged in a water filled aquarium. Under favorable conditions, enough electrical energy can be delivered to the wire that will result in its *burst*, or explosion. The set of experiments we consider here were performed by [9].

It was previously found that a standard lumped circuit consisting of a resistor, inductor, and capacitor (RLC) is representative of the overall dynamics as illustrated in Figure 4-1a [10]. In the circuit, a capacitor with capacitance C_0 is charged to an initial voltage of V_0. Following this, a switch is flipped at the initial time so that current begins to flow through the RLC circuit, which additionally includes a static resistor with resistance R_0 and an inductor with inductance L_0. Additionally, the exploding wire is connected in series to these elements by cabling and grips, which are shown in Figure 4-1b. In the present work the impedance of the cabling and grips is accounted for in the static resistance and inductance. The grips themselves are multi-pronged brass claws that secure the ends of the wire in place once they are tightened. The wire is a metallic cylinder of prescribed length and diameter and is treated as a time-varying resistor in the circuit with a resistance of $R_M(t)$. The wire burst occurs when its electrical resistance dramatically spikes as it undergoes phase transitions, which subsequently alters the circuit dynamics. The burst is also manifested by an impulsive spike in the voltage drop across the wire [10].

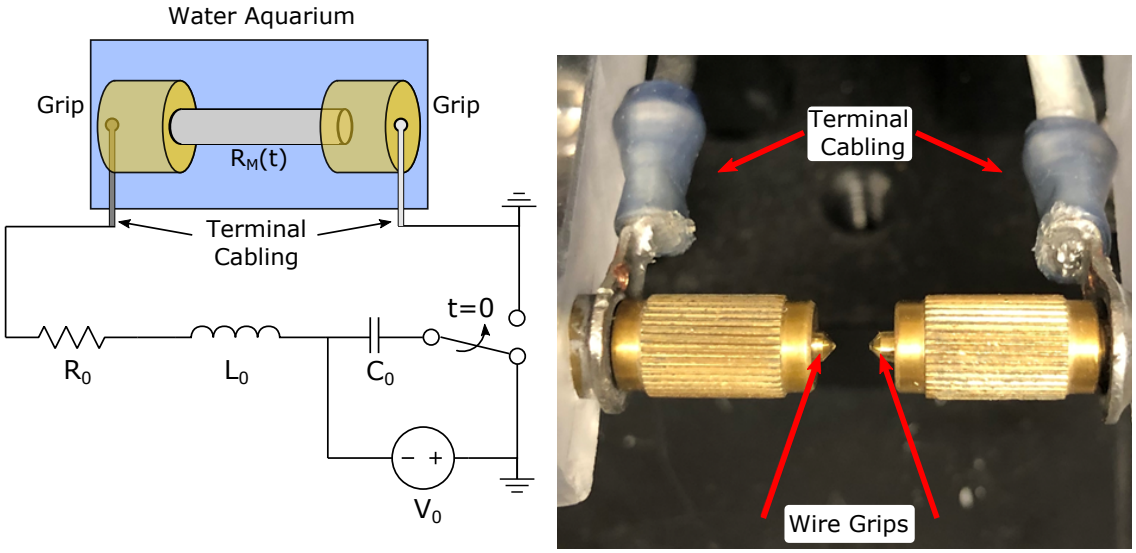

Figure 4-1 Exploding wire electrical setup.
The lumped circuit model is shown on the left while the experimental wire grips and cabling are shown on the right.

In all the experiments, the grips were positioned such that 100 mil (milli-inch) of wire is exposed. The static resistance and capacitance of the circuit were fixed, while the initial voltage, inductance, wire diameter, and wire material were varied. In the present work, only a single wire material (gold) at two different voltage and inductance values will be investigated. Three identical experiments were performed at a voltage of 1500 V and 477 nH inductance, while a single experiment was performed at 2000 V and 450 nH. For simplicity, the 1500 V case will be referred to as the low

voltage case and the 2000 V case as the high voltage case. In order to check the validity of the low-Rm approximation, we estimate an initial magnetic Reynolds number of $R_m \approx 10^{-3} \ll 1$, which decreases rapidly as the electrical conductivity drops.[7] A summary of these and the remaining experimental inputs is given in Table 4-1.

Table 4-1 Exploding wire input parameters.

Parameter	Variable	Value
Wire Length	L_w	100 mil
Wire Diameter	D_w	1.73 mil
Wire Material	-	Gold
Resistance	R_0	235 mΩ
Inductance	L_0	477 & 450 nH
Capacitance	C_0	0.931 μF
Initial Voltage	V_0	1500 & 2000 V

As previously mentioned, the LGR simulations employ an unstructured simplex finite element mesh to discretize the geometry. In this work we present two levels of approximation which will be referred to as two-dimensional (2D) and three-dimensional (3D) approximations. In both approximations, both the wire and the ambient water material are modeled. Since the wire burst will be more or less axisymmetric about the wire length, a quarter symmetry approximation is used in which only a quadrant of the problem is modeled, resulting in the 3D approximation. The 2D approximation further simplifies this by assuming the voltage field solution from (5) will vary linearly along the length of the wire. As a result, only a single plane within the wire can be modeled. In both the 2D and 3D approximations the entire cylindrical wire is accounted for in the circuit. The low-Rm equations are then discretized on these reduced geometrical representations of the wire and the problem is advanced in time as previously described.

An example mesh for both approximations is shown in Figure 4-2. Along with this, a diagram explaining the wire geometry is also shown at the top of the figure. In both approximations, the wire material (grey material) is meshed at a higher resolution compared with the ambient water (blue material). The water material extends sufficiently far from the origin so that any reflected waves will not impact the expanding wire material throughout the time period of interest. The distance that was determined to be sufficient was at $R_o = 256R_w$, with R_0 being the water region's radius and R_w being the wire's initial radius. Also shown in the figure is a third radius R_b, which defines a buffer region where the initial water material is refined surrounding the wire so that the early time dynamics are well captured. For the simulations in this work it was found that the buffer radius can be 1-2 times the initial wire radius.

It is also noted that in addition to the low and high voltage cases, there are two different tabular equation of state models which are employed for the wire material: (i) SESAME and (ii) UTri.

[7] To estimate the magnetic Reynolds number here, we have performed a back of the envelope calculation with values of $L \approx O(10^{-5})$ m representing the wire diameter and $\sigma_e \approx O(10^7)$ S/m. The velocity scale was estimated to be $U \approx O(10^1)$ m/s, which is the approximate wire diameter divided by a time period of $\approx O(1)$ μs, which was computed from the oscillation period of an RLC circuit [7].

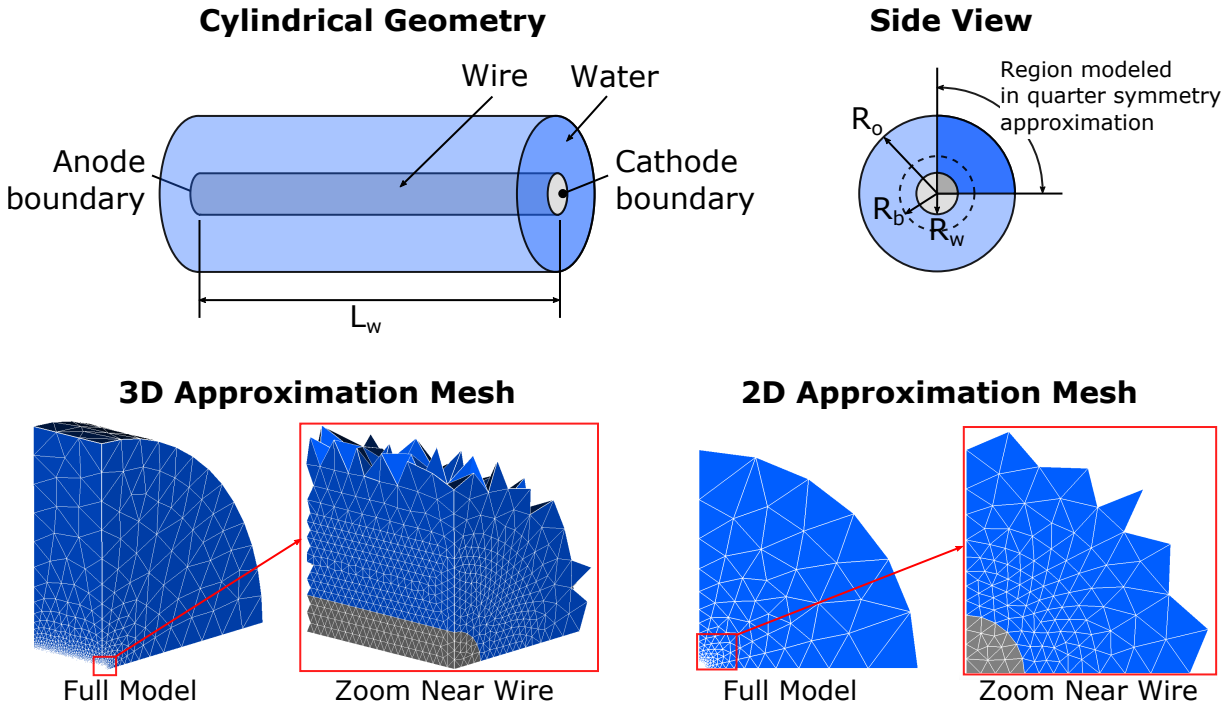

Figure 4-2 Depiction of LGR simulation geometries and modeling approximations.

In either case, the water is modeled using a separate SESAME table and a constant value for the water's conductivity. The initial thermodynamic states for all the materials were set to standard ambient temperature and pressure (SATP) conditions.

4.2. Simulation Results

4.2.1. Mesh Convergence

In order to better separate the various uncertainties in modeling the exploding wire, a mesh convergence study was performed. Three different initial mesh resolutions were used: coarse, medium, and fine. Starting with the coarsest mesh resolution of $\Delta x = D_w/8$, the target edge lengths (Δx) of the simplices were halved to obtain the medium mesh and then halved again for the fine mesh.[8] For each mesh, the current through and voltage across the wire were tracked in time. An example of this output for a 2D approximation is shown in Figure 4-3.

In Figure 4-3, the voltage and current traces for a typical wire burst are shown. The burst occurs when the wire voltage rapidly spikes and then levels off soon after. In the bottom row, the temper-

[8]It is noted that the initial resolution applies to the initial wire and water buffer region. The outside water material was appreciably coarser so as not to incur unnecessary costs. Still, the mesh refinement was performed globally on the entire mesh.

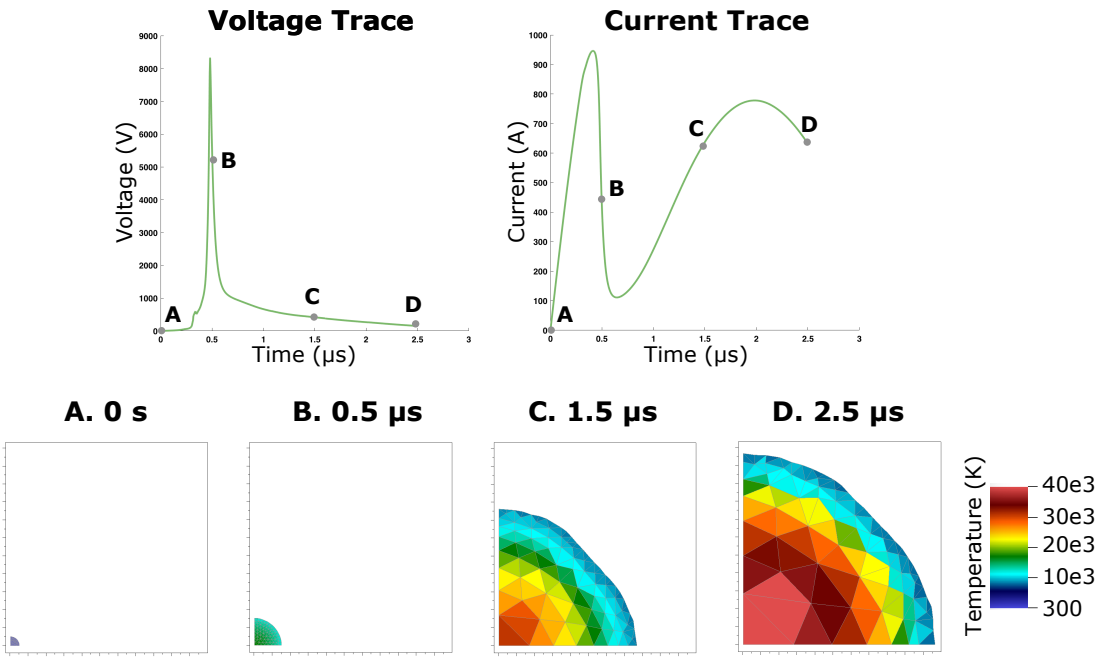

Figure 4-3 Example wire simulation output.
The top row shows the voltage and current traces from a typical 2D wire simulation. The mesh and temperature within the wire is depicted at four different times in the bottom row. Tickmarks are placed in each direction which are spaced apart by the initial wire radius.

ature inside the wire is also shown at different points in time, which are denoted by the letters A through D in the traces. At the initial time, the entire cross section is at ambient temperature. Soon after burst at 0.5 μs, the wire begins to expand at a modest rate as it grows radially by nearly 3 times its original diameter. Following this, the current recovery region begins around 0.75 μs where the current increases again and has a second peak around 2 μs. Around this time and onward, we can see from the temperature contours that the inner core of the wire heats more rapidly than the wire's surface, reaching temperatures greater than 40,000 K, as the wire quickly expands and undergoes phase changes.

Of particular interest in Figure 4-3 is the peak voltage which occurs slightly earlier in time than point B which was at 0.5 μs. The peak voltage can provide a useful single-valued metric which may be used to assess mesh convergence. As a result, we perform LGR simulations using the coarse, medium, and fine meshes, tracking the peak voltage for each. Simulations at the low and high voltage values for the 2D and 3D approximations for each equation of state were performed. The peak voltage metric for every simulation is plotted against the normalized wire diameter, which is the diameter divided by the initial target mesh edge length, in Figure 4-4.

From the figure, it is visually apparent that the peak voltage is converging for nearly all configurations. It appears that the 2D simulations are converging to a slightly higher peak voltage value than the equivalent 3D simulations, which is perhaps a result of the interplay between the spatial dimensions and the artificial viscosity used to stabilize the solver [3]. In the present simulations, values of 0.5 and 1.0 were used in both 2D and 3D for the linear and quadratic viscosity parameters, which

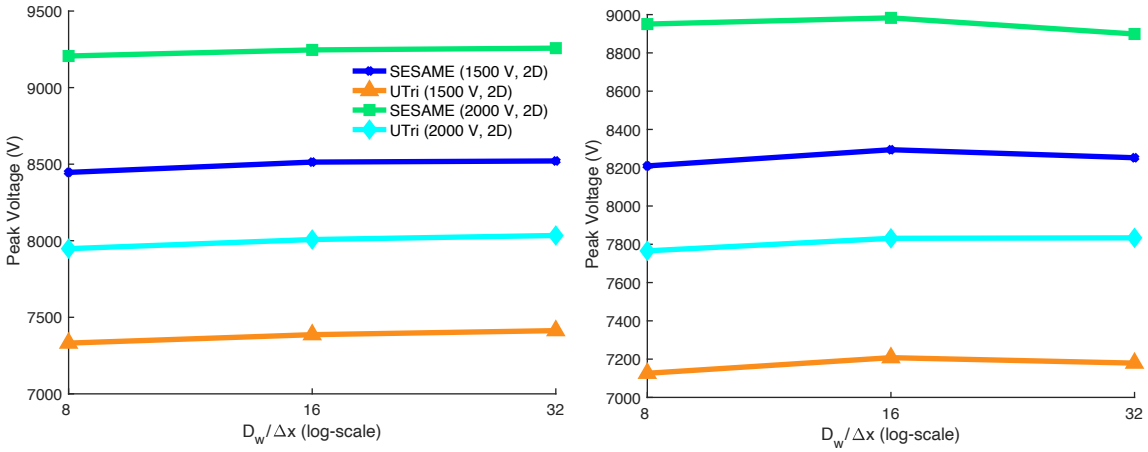

(a) 2D. **(b)** 3D.

Figure 4-4 Peak voltage values in 2D and 3D mesh refinement simulations.

is further investigated in the next section. Additionally, for these particular tables, the UTri table consistently predicts a lower peak voltage than the SESAME table. In order to better quantify the convergence rates, Richardson extrapolation is used to determine the observed convergence rates [11]. For each of the configurations in Figure 4-4, Table 4-2 summarizes the convergence rates. All cases are converging except for one, which is the high voltage SESAME case in 3D. Despite this, the typical convergence rates are mostly within the range of 1.0-1.8. Since it appears that the mesh sizes under consideration mostly fall within the asymptotic regime of convergence, the remaining simulations will use the medium mesh resolution.

Table 4-2 Observed convergence rates from Richardson extrapolation.

Voltage (V)	Wire Material Model	Dimension	Convergence Rate
1500	SESAME	2D	3.2
"	"	3D	1.0
"	UTri	2D	1.1
"	"	3D	1.5
2000	SESAME	2D	1.8
"	"	3D	-
"	UTri	2D	1.2
"	"	3D	4.8

4.2.2. Numerical Parameter Variation

We turn our attention to the effects of variability in the numerical parameters. There are three key numerical parameters in particular that are considered: linear artificial viscosity, quadratic artificial viscosity, and the gradation rate. The viscosity parameters control the amount of artificial damping applied to the governing equations in compressed regions for numerical stability. The gradation rate on the other hand controls how much variation in size there can be between any two adjacent mesh elements. While each of these parameters are described by [3], appropriate values may range from 0.125 - 1.0 for each of the viscosity parameters and 0.5 to 0.9 for the gradation rate. Using the driving software Dakota [12], these parameter ranges were sampled using 40 Latin hypercube samples to explore their effect on the simulation variability. The results of these variations are shown in the figures found in Figure 4-5.

In Figure 4-5 four figures are shown. Figures 4-5a and 4-5c show voltage traces across the wire for the low and high initial voltage configurations, respectfully. Similarly, Figures 4-5b and 4-5d show the corresponding current traces. In both cases, the shaded regions were generated by taking the range of the simulation output data over all the simulations at each instance in time, giving the maximum observed variability. In addition to the simulation data, the filtered experimental traces are also shown. Similar to the simulation data, the ranges were taken to generate a shaded region of possible experimental results. The bounds are most apparent in the low voltage configuration where there were three repeated experiments compared with the single experiment at the higher voltage.

Looking at the low voltage configuration, it is clear that the simulations are over-predicting the voltage peak. However, it was confirmed by the experimental team who originally performed the experiments that the amplitude of the experimental voltage traces are suspect given the physical hardware that was used. Nonetheless, the timing of the voltage is accurate, which includes when the peak voltage occurs. For both the UTri and SESAME models, as well as the 2D and 3D approximations, there was still little variability in the simulation voltage traces, leaving most of the variability to the current traces. Furthermore while there are differences between the 2D and 3D approximations, the different equations of states had a much more significant impact on the current traces, particularly at late times in the current recovery regions. The strongest agreement with the experimental results appears to be with the SESAME equation of state.

5. CONCLUSION

A new methodology for simulation of low magnetic Reynolds number magnetohydrodynamic physics with Lagrangian unstructured finite elements is described. A GPU implementation was performed within the LGR software framework. Verification of the low-Rm equations was performed with multiple test problems. Following this, LGR was applied to an exploding wire problem and compared with experimental data. It was shown that mesh convergence was achieved in the peak voltage metric with each of the approximations that were used. Additionally, it was found that the equation of states resulted in the largest variability when compared with other numerical parameters. We note that the experimental grips securing the wire were not included in either of the

geometric approximations, which may alter the geometric evolution of the wire burst. However, as was earlier demonstrated, sharp geometric changes, which could be realized near the grips, may prove problematic to mesh refinement due to underlying singularities. As a result of these findings, future work can focus on modeling the grips and delving deeper into more detailed analysis of the different equations of state.

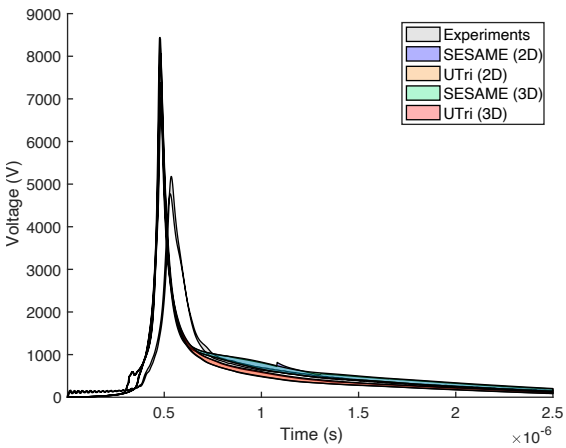

(a) Voltage trace at 1500 V.

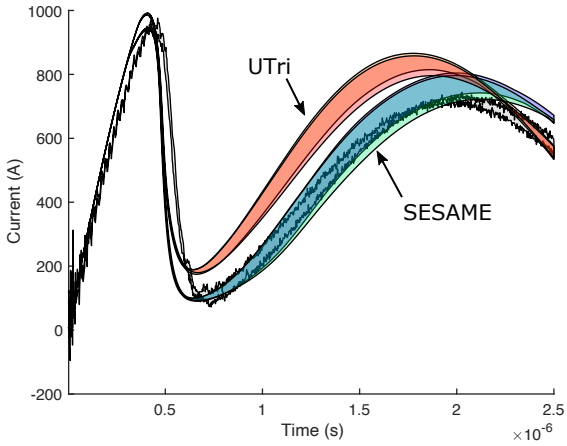

(b) Current trace at 1500 V.

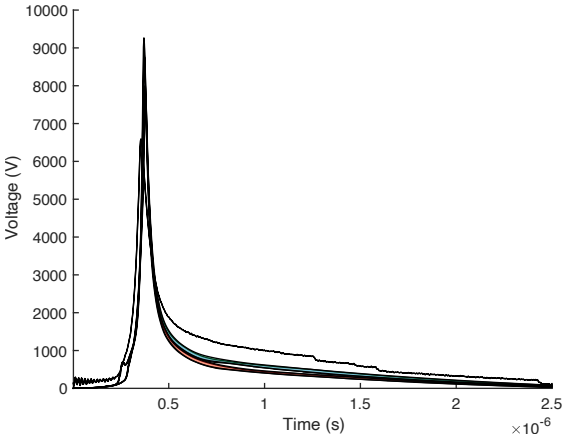

(c) Voltage trace at 2000 V.

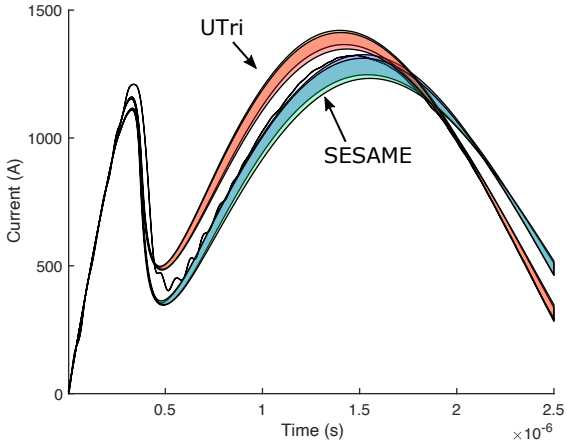

(d) Current trace at 2000 V.

Figure 4-5 Voltage and current traces for different initial voltages under parameter variation.

REFERENCES

[1] P. A. Davidson. *Introduction to Magnetohydrodynamics*. Cambridge University Press, 2 edition, 2017.

[2] A. Robinson, T. Brunner, S. Carroll, R. Drake, C. Garasi, T. Gardiner, T. Haill, H. Hanshaw, D. Hensinger, D. Labreche, R. Lemke, E. Love, C. Luchini, S. Mosso, J. Niederhaus, C. C. Ober, S. Petney, W. J. Rider, G. Scovazzi, O. E. Strack, R. Summers, T. Trucano, V. G. Weirs, M. Wong, and T. Voth. ALEGRA: An arbitrary Lagrangian–Eulerian multimaterial, multiphysics code. In *46th AIAA Aerospace Sciences Meeting and Exhibit*, page 1235, 2008.

[3] D. A. Ibanez, E. Love, T. E. Voth, J. R. Overfelt, N. V. Roberts, and G. A. Hansen. Tetrahedral mesh adaptation for Lagrangian shock hydrodynamics. *Computers & Mathematics with Applications*, 78(2):402–416, 2019.

[4] W. C. Swope, H. C. Andersen, P. H. Berens, and K. R. Wilson. A computer simulation method for the calculation of equilibrium constants for the formation of physical clusters of molecules: Application to small water clusters. *The Journal of Chemical Physics*, 76(1):637–649, 1982.

[5] S. Lyon and J. Johnson. SESAME: The Los Alamos national laboratory equation of state database. Technical Report No. LA-UR-92-3407, Los Alamos National Laboratory, Los Alamos, NM (United States), 1992.

[6] J. Carpenter. EOS table interpolation a brief overview and my path. JOWOG32MAT EOS Workshop, 2016.

[7] J. D. Irwin and R. M. Nelms. *Basic Engineering Circuit Analysis*. Wiley, 10 edition, 2010.

[8] J. D. Jackson. *Classical Electrodynamics*. Wiley, New York, 3 edition, 1999.

[9] J. D. Olles, C. J. Garasi, and J. P. Ball. Quantitative details of exploding wires with application to single pore collapse validation. Technical Report SAND2018-7148C, Sandia National Laboratories, Albuquerque, NM (United States), 2018.

[10] P. O'Malley and C. J. Garasi. Understanding the electrical interplay between a capacitive discharge circuit and exploding metal. Technical Report SAND2015-1132, Sandia National Laboratories, Albuquerque, NM (United States), 2015.

[11] P. J. Roache. Quantification of uncertainty in computational fluid dynamics. *Annual Review of Fluid Mechanics*, 29(1):123–160, 1997.

[12] B. M. Adams, W. J. Bohnhoff, K. R. Dalbey, M. S. Ebeida, J. P. Eddy, M. S. Eldred, G. Geraci, R. W. Hooper, P. D. Hough, K. T. Hu, J. D. Jakeman, M. Khalil, K. A. Maupin, J. A. Monschke, E. M. Ridgway, A. A. Rushdi, J. A. Stephens, L. P. Swiler, D. M. Vigil, T. M. Wildey, and J. G Winokur. Dakota, a multilevel parallel object-oriented framework for design optimization, parameter estimation, uncertainty quantification, and sensitivity analysis: Version 6.13 user's manual. Technical Report SAND2014-4633, Sandia National Laboratories, Albuquerque, NM (United States), 2014, updated 2021.

DISTRIBUTION

Email—Internal

Name	Org.	Sandia Email Address
Technical Library	1911	sanddocs@sandia.gov

Sandia National Laboratories

Sandia National Laboratories is a multimission laboratory managed and operated by National Technology & Engineering Solutions of Sandia LLC, a wholly owned subsidiary of Honeywell International Inc., for the U.S. Department of Energy's National Nuclear Security Administration under contract DE-NA0003525.